

X-RAY FLARE DRIVEN CHEMISTRY IN PLANET FORMING REGIONS

Abygail R. Waggoner

Advisor: L. Ilse-dore Cleeves

University of Virginia, Department of Chemistry

Abstract: Planet formation begins when a molecular dust cloud collapses in on itself to form a young, central star surrounded by a disk of dust and gas known as a protoplanetary disk. T-Tauri stars, or young sun-like stars, are X-ray bright, where the emitted X-ray photons drive chemical evolution in the disk via ionization of H_2 . Typically X-ray emission, and therefore disk ionization levels, is considered constant on time scales less than thousands of years. However, T-Tauri stars are known to be X-ray variable on short time scales (days to weeks) via X-ray flaring events. We model the chemical responses to flares over the course of 500 years. We find that flares have both a cumulative impact on disk chemistry, resulting in a new pseudo steady state, and a short-term impact, resulting in stochastic abundances on observationally relevant time scales (days to weeks).

1. INTRODUCTION

Protoplanetary disks are formed after a molecular cloud gravitationally collapses, forming a pre-main sequence (PMS) star surrounded by a chemically rich^[1–5] and physically dynamic^[6] disk where planet formation occurs. To understand not only the formation of planets, but also the chemical compositions of the planets' terrain and atmosphere, we must be able to accurately model the chemical and physical processes that occur in the protoplanetary disk's complex environment^[7,8].

1.1. Chemical and Physical Structure

A typical protoplanetary disk has a radius of tens of astronomical units (au) with a total mass of $\sim 0.04 M_{\odot}$ ^[10], but larger disks can span hundreds of au with masses up to $\sim 0.2 M_{\odot}$ ^{e.g.[11]}. Recent studies from the Disk Substructure at High Angular Resolution Project (DSHARP) have shown that disks can, and are likely to, have substructure, such as rings or gaps, spiral arms, and misaligned rings^{e.g.[12–15]}. This complex physical structure results in the presence of a broad range of molecular and atomic species. The physical and chemical structure of a disk is described by three layers: *i.* the photon-dominated region, the outermost layer that is rich in atomic and ionic species, *ii.* the warm molecular layer, the middle layer that is dominated by gaseous molecular and radical species^[1], and *iii.* the mid-plane, the innermost layer composed primarily of dust grains and molecular and atomic ices (Figure 1^[9]).

The majority of observed species are small and simple molecules, such as CO , HCO^+ , CN , H_2O , OH , CO_2 , HCN , CS , C_2H , and N_2H^+ ; however, a number of more complex molecules, such as formaldehyde, methanol, and

methyl cyanide have also been detected^[2–5,16]. Ref. [17] provides a census of all detected molecules as of 2018, but the past year has led to the discovery of even more molecules^{e.g.[18–20]}. Historically, chemistry is thought to evolve slowly, over the lifetime of the disk (millions of years)^[21–24], but short-term (days to years) chemical evolution has been relatively unexplored. As detection methods and telescopes are becoming more efficient at detecting larger molecules and relatively less abundant species at higher resolutions, we must determine whether it is accurate to assume chemistry is constant over observational time scales, or if it is possible for external factors, such as radiation, to result in short-term variability.

1.2. Central Star

Perhaps one of the most important features of a protoplanetary disk is the central PMS star. T-Tauri stars are a typical PMS star studied in protoplanetary disks, as they are common and follow the same evolutionary track as the Sun. T-Tauri stars are highly variable in the X-ray regime due to X-ray flaring produced by magnetic reconnection events on roughly a weekly basis^{e.g.[25]}. On the stellar surface, magnetic loops can be as large as several stellar radii^[26] and can trap hot ionized gas, which radiates X-ray photons at nearly a constant rate defined as the characteristic, or baseline, X-ray luminosity (L_{char}). When two magnetic loops undergo magnetic reconnection, the gas is heated up to millions of Kelvin, resulting in a burst of X-ray radiation known as an X-ray flare^[26]. As a star ages, the stellar dynamo stabilizes and magnetic fields are thought to become less intense and frequent, so the star experiences less intense X-ray radiation (Review [27] and citations therein). In order to best understand the earliest stages of our Solar System, we must first

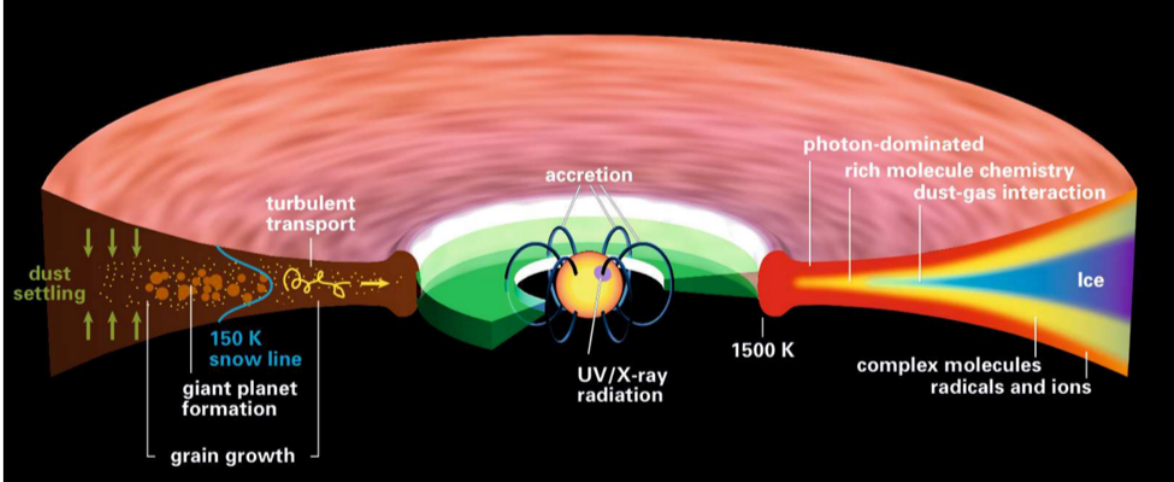


Figure 1. From ref. [9]. Protoplanetary disks are diverse in both chemical and physical structures. Dust settling occurs in the inner midplane, where temperatures drop low enough for ices to form on the dust grains. Planet formation occurs within these snow lines.

understand how the highly variable radiation of “young Suns,” like T-Tauri stars, affects the protoplanetary disk environment.

1.3. Influence of Stellar Radiation on Chemistry

The high levels of radiation emitted by T-Tauri stars are known to shape the disk temperature and density distribution through low energy emission^[28] (e.g. IR and optical) and to drive disk chemistry through ionization by high energy emission^[21–24] (e.g. UV and X-rays). X-ray emission is of particular interest, as X-ray photons are capable of penetrating the inner layers of the disk, while UV photons are absorbed along the disk surface. Thus, X-rays have the potential to drive chemistry at greater disk depths^[29,30]. X-ray ionization occurs via the ionization of H_2 ^[31], which results in the formation of H and H_3^+ both of which are essential in the formation of more complex molecules^{e.g.[26]}.

Currently, it is considered typical for protoplanetary disk models to include a single characteristic X-ray ionization rate. However, it is still unknown how a time variable X-ray ionization rate affects disk chemistry. Recent observations by ref. [32] suggest that X-ray flaring is a likely source of chemical variability within protoplanetary disks based upon Atacama Large Millimeter/submillimeter Array (ALMA) observations of significant (20σ) variability in H^{13}CO^+ , a known X-ray sensitive molecule. During the course of my graduate studies, I aim to use a combination of theory and observations to explore both *i.* the observational implications of short-term (days) chem-

ical variability in response to discrete flaring events, and *ii.* the long-term (years to thousands of years), cumulative impact of stochastic flaring on global chemical abundances.

2. MODEL

2.1. X-ray Light Curve Generator: *XGEN*

To create synthetic X-ray light curves for use with the chemical model, we created a flexible code for generating randomized light curves drawing from known stellar X-ray flare statistics. The code, called the X-ray Light Curve Generator (*XGEN*), models a stochastic light curve based on a user provided total flare frequency, flare energy distribution, and rise/decay time. Literature has shown that the energy distribution of stellar flares in an X-ray light curve can be defined by a power-law distribution:

$$\frac{dN}{dE} = \beta \log(E_{\text{tot}})^{1.0-\alpha}, \quad (1)$$

where the power-law defines the total number of flares (dN) that occur over an energy range (dE).

There are a number of flare simulations done in the past^{e.g.[33]}, but these simulations typically generate a light curve in units of count rate or are designed to specifically replicate individual or small sets observed flares. *XGEN* works directly in luminosity. In this work luminosity is calculated in erg second^{-1} , but *XGEN* can create a light curve in any user specified energy unit.

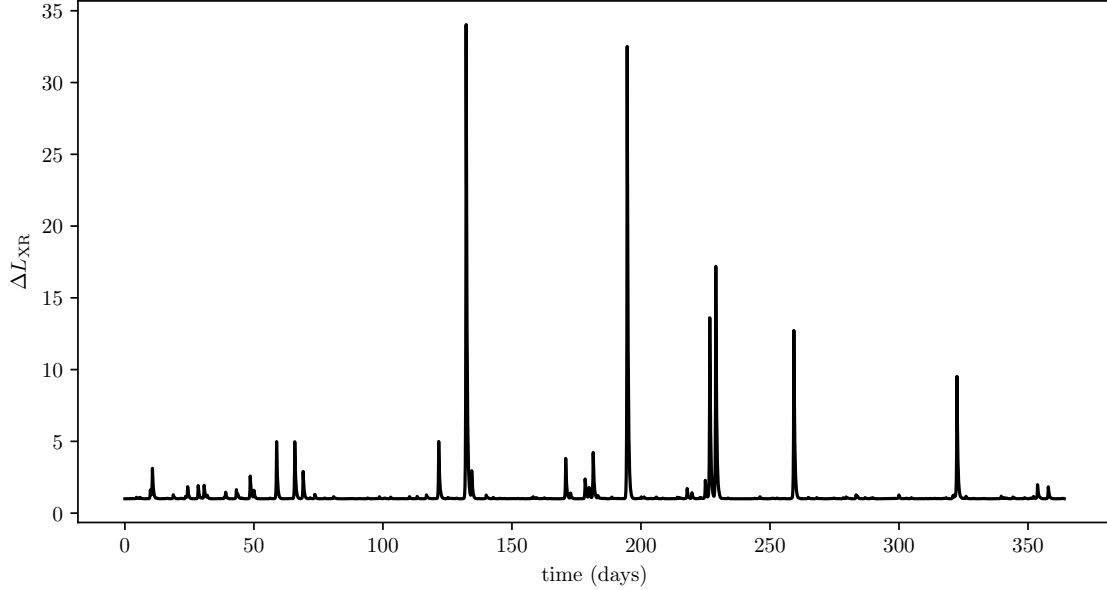


Figure 2. A typical X-ray light curve for a T-Tauri star modeled by *XGEN*. ΔL_{XR} is the relative change in luminosity when there is a flare compared to the characteristic luminosity (Equation 5).

A typical light curve generated by *XGEN* for a T-Tauri star is shown in Figure 2, but we note that *XGEN* is not limited to an X-ray light curve produced by a T-Tauri star. Instead, *XGEN* can create any light curve based on a power law distribution, including but not limited to flares from main sequence stars and AGN.

2.1.1. Overview of Model: *XGEN* uses a random number generator to determine the probability that a flare with total energy E_{tot} will occur. The random number generator uses the python 2.7 numpy.random package, version 1.16.6 and build py27hbc911f0_0. The probability of a flare with energy E_{tot} occurring is defined by

$$P(E_{tot}) = \beta (E_2^{-\alpha+1} - E_1^{-\alpha+1}) \quad (2)$$

$$\beta = -\mathcal{F} E_{min}^{\alpha-1} \Delta t \quad (3)$$

where β is a normalization constant, \mathcal{F} is the target flare frequency, Δt is the time step resolution ran in *XGEN*, and flare frequency is the average observed number of flares that occur within a set time frame. Multiple flares are allowed to occur within the same time step, which, like in reality, could represent flares occurring on different parts of the star, for example.

All flares are assumed to have an exponential rise (τ_{rise}) and decay (τ_{decay}) time profile. *XGEN* is written such that τ_{rise} and τ_{decay} can be variable based on a probabil-

ity distribution, but for the purposes of this paper, we assume a uniform $\tau_{rise} = 3$ hr and $\tau_{decay} = 8$ hr for all flares. Individual flare shapes are defined by Equation 4, where E_{tot} is determined by the random number generator (Equation 2), and ΔL_{peak} is calculated in the model. Figure 3 demonstrates the construction of a single flare.

$$E_{tot} = \Delta L_{peak} \int_{-\infty}^{t_{peak}} e^{t/\tau_{rise}} dt + \Delta L_{peak} \int_{t_{peak}}^{\infty} e^{-t/\tau_{decay}} dt \quad (4)$$

The light curve is constructed by adding the luminosity of all flares at every time step, then adding the characteristic luminosity (L_{char}). For the purpose of this study, light curves are also normalized with respect to L_{char} (Equation 5).

$$\Delta L_{XR} = \frac{\sum L_{flare} + L_{char}}{L_{char}} \quad (5)$$

XGEN includes flares that are lower than presently detectable, e.g., microflaring and nanoflaring events. Therefore many of the individually modeled flares overlap or are below a realistic detection limit. As a result, we define ‘observable flares’ as those that satisfy two criteria. First, the flare peak must be distinguishable. *XGEN* identifies individual flare peaks as any point where the slope is effectively zero ($|dL_{XR}/dt| < 0.015$). Once individual flare peaks are identified, the beginning and end of each flare is

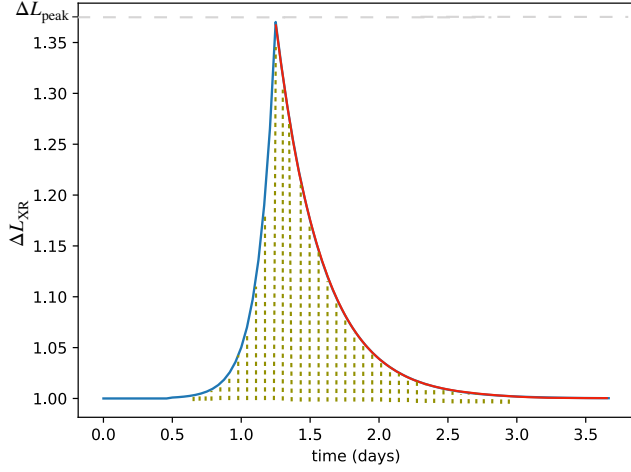


Figure 3. An individual flare modeled by *XGEN*. Flare shape is determined by Equation 4, where the total flare energy (E_{tot} , dashed green lines) is determined via a random number generator. The flare rise (blue line) and flare decay (red line) are constructed from τ_{rise} and τ_{decay} , respectively. The flare peak (ΔL_{peak}) is calculated by *XGEN*.

determined by a location where the slope either returns to zero or switches signs. This process constructs each distinguishable flare. Second, the distinguishable flare must have a total energy greater than a predetermined minimum energy value ($E_{\text{min,obs}}$) to be considered observable. *XGEN* can then determine energy distribution and frequency of observable, distinguishable flares, which can then be compared to an observed energy distribution.

2.1.2. X-ray Light Curve for a T-Tauri Star: The light curves presented in this work are modeled after the statistical analysis of solar mass PMS stars presented in [25]. The data presented in ref. [25] are from the *Chandra Orion Ultra-Deep Project (COUP)*. The *COUP* survey is the longest, continuous observation of stars in the X-ray regime, thus making it the most comprehensive study of X-ray flaring events in solar mass stars to date. The energy distribution of flares observed by ref. [25] are best fit by

$$N = 1.1 \log(E_{\text{tot}})^{-0.66} \quad (6)$$

where N is the cumulative number of flares observed with total energy E_{tot} or greater and $\alpha = 1.66$. The reported average flare frequency was approximately 1 flare every 650 ks, with an uncertainty of 10%, or ~ 50 flares per year.

Flares modeled by *XGEN* range from $E_{\text{min}} = 10^{32.50}$ erg to $E_{\text{max}} = 10^{37.54}$ erg. Observable flares are considered

Quantity	Symbol	Value
Parameters from ref. [25]		
Max Observed Flare Energy	E_{max}	$10^{37.57}$ erg
Min. Observed Flare Energy	$E_{\text{min,obs}}$	$10^{34.0}$ erg
Characteristic Luminosity	L_{char}	$10^{30.25}$ erg
Target Flare Frequency	\mathcal{F}	48.5 yr^{-1}
Flare rise time	τ_{rise}	3.0 hrs
Flare decay time	τ_{decay}	8.0 hrs
Parameters found to produce best fit energy distribution		
Power-law index	α	1.64
Min. modeled flare energy	$E_{\text{min,model}}$	$10^{32.50}$ erg
Energy Step Resolution	ΔE	$10^{0.01}$ erg
Time Step Resolution	Δt	60 min

Table 1. Input parameters used to generate an X-ray flare light curve for a T-tauri star.

* parameters based on a statistical analysis of PMS solar mass stars presented in [25].

** parameters found to produce the best fit energy distribution (Figure 4).

those that are consistent with the definition of an observed flare in ref. [25]. The minimum total energy for an observable flare was set to E_{tot} of the weakest flare reported in ref. [25], $E_{\text{min,obs}} = 10^{34.0}$ erg. The maximum allowed flare energy in the model is consistent with the largest flare energy detected in ref. [25] ($E_{\text{tot}} = 10^{37.57}$ erg). The characteristic luminosity is set to $\log L_{\text{char}} = 30.25$ erg, which is in agreement with previous observations. Flare rise and decay times were set by $\tau_{\text{rise}} = 3$ hr, effectively instantaneous, and $\tau_{\text{decay}} = 8$ hr, the average decay reported in ref. [25].

Light curves were generated with α values ranging from 1.5 to 3.0, where 100 one year curves were ran for each α value. The energy distribution of observable flares is highly sensitive to the chosen α value, as shown in Figure 4. We find that $\alpha = 1.64$ yielded the best overall fit to the observed energy distribution of solar mass young stellar objects (YSOs)^[25] with $\chi^2 = 0.15$. This power law index is consistent with the best fit curve (Equation 6, $\alpha = 1.66$) reported in ref. [25]. It should be noted that $\alpha = 1.50$ appears to better fit the observed distribution below $E_{\text{tot}} \sim 10^{34.5}$ erg. However, α values less than 1.64 fail to fit the high energy flares and have higher χ^2 values. For example, $\chi^2 = 0.91$ for $\alpha = 1.50$.

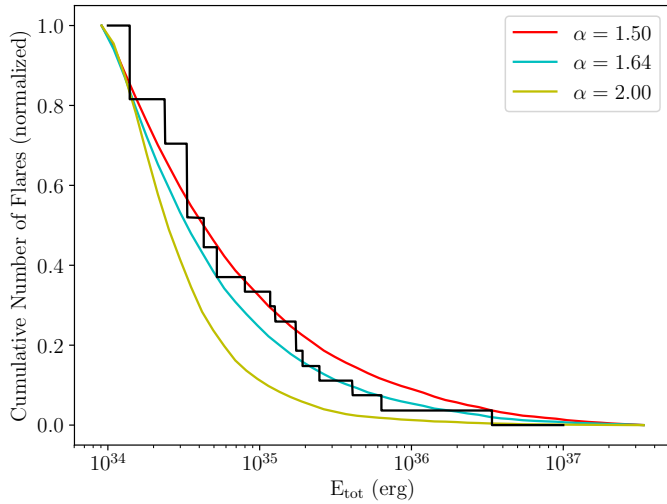


Figure 4. Energy distribution of flares in a T-tauri star. The target observed distribution (see ref. [25], Figure 9) is represented by a black histogram. The best fit is defined by Equation 6. *XGEN* was used to model 100 one year light curves for individual values of α . The flare energy distribution for $\alpha = 1.50, 1.64,$ and 2.00 are shown. $\alpha = 1.64$ was found to yield the best fit energy distribution.

2.2 Disk Chemical Model

The chemical disk model used in this work is modeled after ref. [34]. The physical environment is modeled after the IM Lup protoplanetary disk^[11], the original source observed to experience variability^[32]. The stellar parameters for the central star are considered typical for a T-Tauri star. The chemical model adopts the rate equation method and includes 644 chemical species and 5944 types of chemical and physical processes.

A two dimensional disk is simulated by running point locations at various radial distances (R) and vertical heights (Z). Modeled radial distances include $R = 1.0, 5.0, 10.0, 20.0, 30.0, 40.0, 60.0, 80.0,$ and 100.0 au from the central star. Modeled vertical heights ranged from the disk mid-plane to the disk surface with vertical height ratios of $Z/R = 0.0, 0.1, 0.2, 0.3, 0.4, 0.5,$ and 0.6 .

The model begins with chemical abundances considered typical for a molecular cloud^[35]. A pseudo steady state is reached by running the the model for 0.5 Myr, when X-ray flaring events produced by *XGEN* are initiated. Once flaring begins, defined as $t = 0.0$, the model is run for 500 years at four hour time step resolution. Disk density, temperature, UV ionization, and X-ray ionization are the same as those used and tabulated by ref. [36]. The model

uses a cosmic ray ionization rate of $\zeta = 2.0e - 20s^{-1}$. We note this value is lower a typical $\zeta = 1e - 17s^{-1}$, but $\zeta = 2.0e - 20s^{-1}$ is more consistent with cosmic ray ionization rates seen in denser regions, such as a disk mid-plane (e.g. sources).

X-ray flares are incorporated into the chemical disk network by uniformly increasing the X-ray ionization rate by ΔL_{XR} (Eq. 5) during flaring events. An increase in ionization rate is considered both azimuthally symmetric and symmetric about the mid-plane. This assumption is likely fine because coronal mass ejections (and by extension X-ray flares) are known to wrap around the star. The wrapping results in a uniform photon impact on the disk (sources). The observed increase in $H^{13}CO^+$ in IM Lup supports this theory, as enhancement was the same in both blue and red shift^[32].

2.3. Assessment of Chemical Variability

To best understand the impact of flares on chemistry in the protoplanetary disk the column density (N) and integrated number of each species (\mathcal{N}) was calculated at 1 day resolution from species abundance at the modeled point locations (n). Column density is found by $N = 2.0 \int ndZ$, assuming symmetry about the mid-plane. The integrated number of each species is found by $\mathcal{N} = 2\pi \int NdR$, assuming azimuthal symmetry. Both N and \mathcal{N} incorporate light travel time as the flare propagates through the disk. As a reference, the disk integrated hydrogen is $\mathcal{N}_H = 10^{55}$. Species with $\mathcal{N} < 10^{25}$ (fractional abundance w.r.t. H 10^{-30}) are considered below the error of the model are omitted from the following analysis.

A species' susceptibility to individual flares, i.e. the short-term (days) variability, is quantified by the standard deviation of \mathcal{N} over time. A large standard deviation is indicative of a highly variable species, and a small (e.g. < 0.01) standard deviation indicates that species is not impacted by individual flares. The cumulative impact of many flares, i.e. the long-term (centuries) impact, is quantified by a relative change in abundance ($\Delta\mathcal{N}$).

$$\Delta\mathcal{N} = \frac{\mathcal{N}_0}{\mathcal{N}_{\text{final}}} \quad (7)$$

$\Delta\mathcal{N} > 1.0$ indicates an increase and $\Delta\mathcal{N} < 1.0$ indicates a decrease in abundance as a result of flares. $\Delta\mathcal{N} = 1.0$ suggests that species is unaffected by 500 years of stochastic flares.

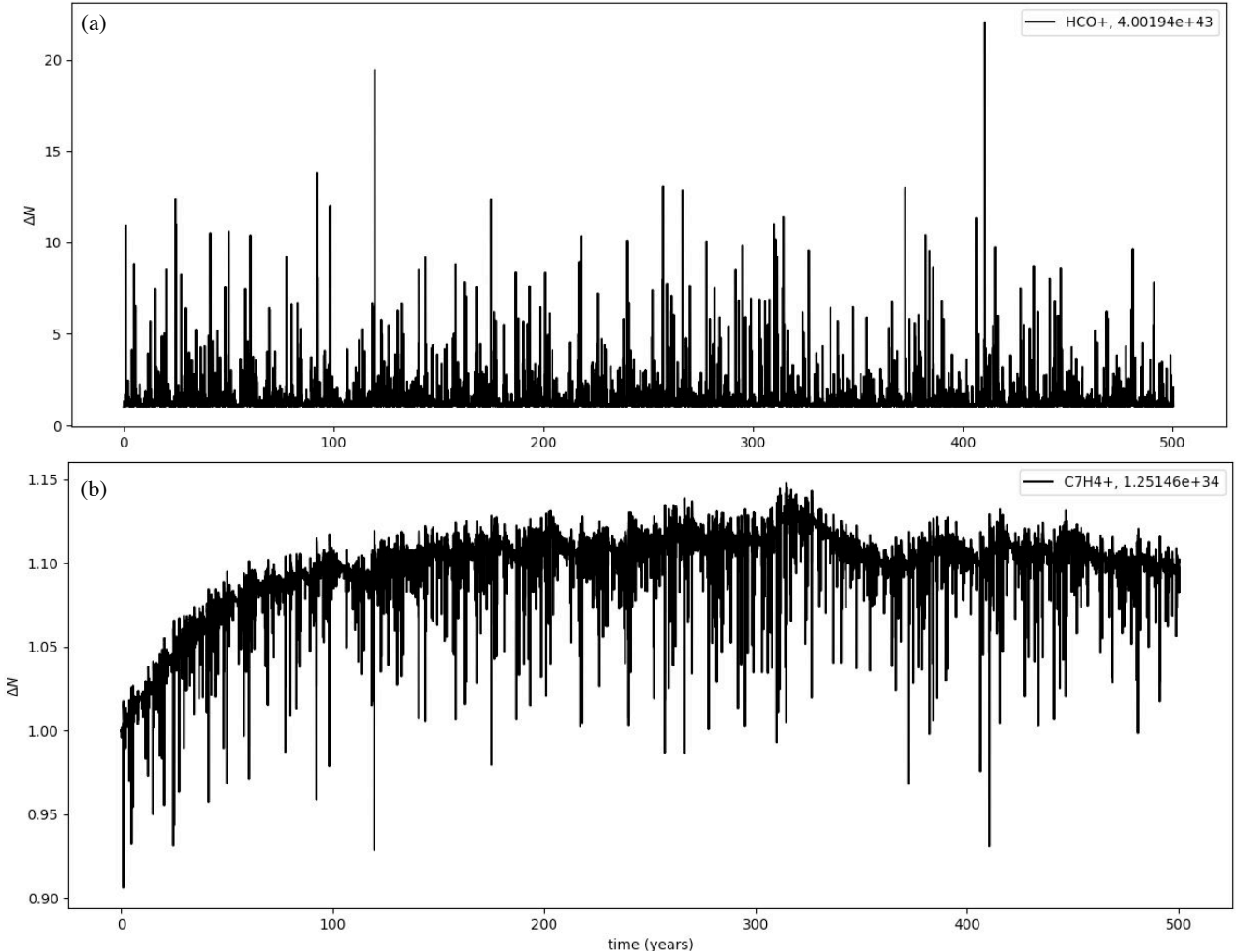


Figure 5. Relative change in disk integrated abundance ($\Delta\mathcal{N}$) as a result of X-ray flaring. \mathcal{N} is defined by Equation 7 and is given in the legend. a.) $\Delta\mathcal{N}$ of HCO^+ . Note that HCO^+ is variable on short time scales (days to weeks) as a result of individual flaring events, but the quiescent HCO^+ abundance is relatively constant. b.) $\Delta\mathcal{N}$ of C_7H_4^+ . Note that C_7H_4^+ has a week response to discrete flaring events, but the quiescent C_7H_4^+ abundance gradually increases by $\sim 10\%$. This suggests a new chemical ‘steady-state’ is reached due to the cumulative impact of many flares.

3. PROGRESS TO DATE

3.1. Overview of Flare Driven Chemistry

Chemical responses to X-ray flaring events fall into three categories. First are flare sensitive species, defined as species whose abundance varies as a direct result of an individual flare. Flare sensitivity is measured by standard deviation ($\sigma > 0.05$), where the most sensitive species have large σ values. Flare sensitive species are considered variable on days to weeks long time scales (Figure 5a). Second are species with altered quiescent states, which are species with an altered ‘steady-state’ abundance as a result of the cumulative impact of many flares over the 500 year model. Altered steady state is measured

by the relative change in abundance ($\delta > 5\%$). A larger percent change corresponds to a more significant impact on the disk integrated chemistry. These species appear to be gradually impacted over hundreds of years resulting in a new pseudo steady state (Figure 5b). Third are species that are non-responsive to flares. These species have $\sigma \sim 0.0$ and $\delta \sim 1.0$.

Of the relatively abundant species ($\mathcal{N} > 10^{25}$) only 24% have σ or $\delta > 1\%$ and only 14% have σ or $\delta > 5\%$. The majority of species in the model are unaffected by flares. Approximately 10% of species are considered significantly variable ($\sigma > 0.05$), and 8% of species have an altered steady state ($\delta > 5\%$). In the following sections, we explore the significance of flare history when consider-

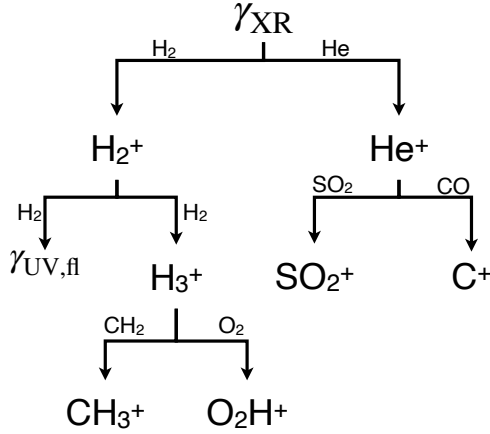


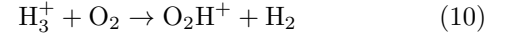
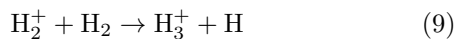
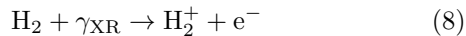
Figure 6. Flare susceptible species (H_2^+ , H_3^+ , SO_2^+ , O_2H^+) and example products. γ_{XR} indicates X-ray photons and $\gamma_{\text{UV,fl}}$ are fluoresced UV photons. When a flare occurs, the X-ray flux increases, then increasing the ionization rates of H_2 and He , and causing a temporary enhancement in gas-phase cations.

ing variable species and provide a more in depth analysis of chemical responses to flares.

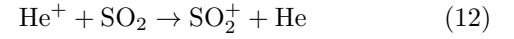
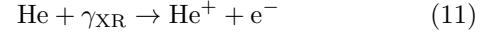
3.2. Cations: The Most Flare Receptive Species

Cations are the most responsive group of species observed in the model. Cations are more likely to experience both an immediate response to flares, and they are more likely to impacted on longer time scales (months) as a result of a single, strong, flaring event. Relatively abundant ($\mathcal{N} > 10^{25}$) gas-phase cations make up $\sim 34\%$ of the chemical network. 77% of the modeled cations have a $\sigma < 5\%$, and 57% have a $\sigma < 1\%$.

Among the flare sensitive cations, H_3^+ , H_2^+ , SO_2^+ , and O_2H^+ are significantly more variable than any other species in the network. These four species, defined as flare susceptible species, are seen to increase by up to 500% in abundance in response to strong flares. H_2^+ is produced from the direct ionization of H_2 from an X-ray photon, thus the increase in H_2^+ abundance is a direct result of the flare enhanced X-ray ionization rate. H_2^+ drives further reactions, leading to the enhancement in H_3^+ and O_2H^+ , as shown in reactions below. Additionally, H_2^+ can collisionally de-excite with H_2 , resulting in the fluorescence of a UV photon ($\gamma_{\text{fl,UV}}$).



Enhancement of SO_2^+ is a result of X-ray ionization of helium, rather than H_2 , as shown in the reactions below. An example reaction network of flare receptive species is shown in Figure 6.



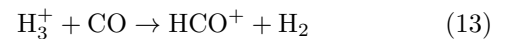
In general, all flare responses can be traced back to the ionization of H_2 and He , where the immediate by products (e.g. $\gamma_{\text{UV,fl}}$, H_3^+ , CH_3^+ , C^+) drive all other chemical variability in the disk. This suggests that the four flare susceptible species are the main drivers in flare driven chemistry.

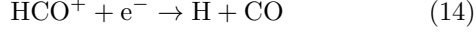
3.3. Neutral Species

There are a total of 324 neutral species in the chemical network, including both the gas and ice phases. However, the vast majority of neutral species are unaffected by flaring events. Only eight of the neutral species have a $\sigma > 1\%$, and only 16 have $\delta > 1\%$. In this section, we highlight the chemical and physical processes that drive variability in these species.

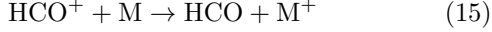
The eight variable neutral species are $\text{H}_{(\text{ice})}$, HCO , O_2H , C_3O , C_2H_4 , C_3H_4 , $\text{CH}_3\text{C}_3\text{N}$, and $\text{C}_2\text{H}_5\text{OH}$. We note that $\text{CH}_3\text{C}_3\text{N}$ and $\text{C}_2\text{H}_5\text{OH}$ networks are incomplete, as this model focuses primarily on gas-phase processes and does not include formation of larger COMS in ice layers. Thus, species known to form primarily in the ice phase, such as $\text{CH}_3\text{C}_3\text{N}$ and $\text{C}_2\text{H}_5\text{OH}$, should be considered with caution. Increase in abundance $\text{H}_{(\text{ice})}$, HCO , O_2H , C_3O , C_2H_4 , and C_3H_4 can be traced to enhancement of H_3^+ from Reaction 9.

$\text{H}_{(\text{ice})}$ is temporarily enhanced in regions from $R = 5$ to 60 au and $Z/R = 0.1$ to 0.3, but remains unaffected throughout the rest of the disk. Gas-phase H production increases Production of gas-phase H increases during a flare primarily from direct production of H_3^+ from H_2 (Reaction 9), but also from dissociative recombination of HCO^+ (Reactions 13 and 14). The increase in H production rate results in faster freeze-out times, thus temporarily increasing the $\text{H}_{(\text{ice})}$ abundance. When a flare ends, hydrogen desorbs back to the gas-phase to return to its pre-flare abundance.



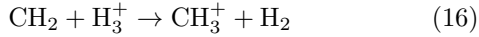


HCO variability occurs primarily beyond $R = 5$ au and within the vertical heights $Z/R = 0.2$ and 0.3 . The main HCO production process is via electron exchange with a metal, such as Mg or Fe (Reaction 15).

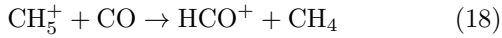
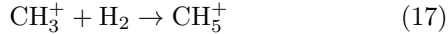


HCO is relatively constant in the disk surface, where UV photolysis and destruction reactions with cations are significantly faster than the neutralization of HCO^+ . Between $Z/R = 0.2$ and 0.3 HCO enhancement closely follows HCO^+ enhancement. Below $Z/R = 0.2$, HCO is not significantly abundant.

The remaining variable neutral species can be traced to production of CH_3^+ from protonation of CH_2 (Reaction 16).



In the upper layers of the disk beyond the water snow-line, oxygen bearing species persist in the gas-phase and rapidly react with CH_3^+ driving variability in oxygen bearing species, such as O_2H . In the inner layers of the disk, within the water snow-line, CH_3^+ is able to persist long enough to combine with H_2 to form CH_5^+ (Reaction 17). CH_5^+ then then protonates CO to form HCO^+ and CH_4 (Reaction 18).



C^+ , a flare enhanced species (Figure 6), and CH_4 drive variability in a carbon bearing species, such as the variable neutral species C_2H_4 , C_3H_4 , and C_3O , as demonstrated in Figure 7

4. CONCLUDING REMARKS

T-Tauri stars, or baby suns, are X-ray variable due to magnetic reconnection events on the stellar surface. Dynamic X-ray emission results in variable X-ray ionization rates, and therefore time variable chemistry in the surrounding protoplanetary disk. In this work, we model flare driven chemical variability by assessing the short-term (days-weeks) and long-term (hundreds of years) variability of chemical species. To do so, a new X-ray flare model, *XGEN*, was written. *XGEN* produces a light curve, which is then incorporated into a chemical disk model. We find that X-ray flares dominantly affect gas-

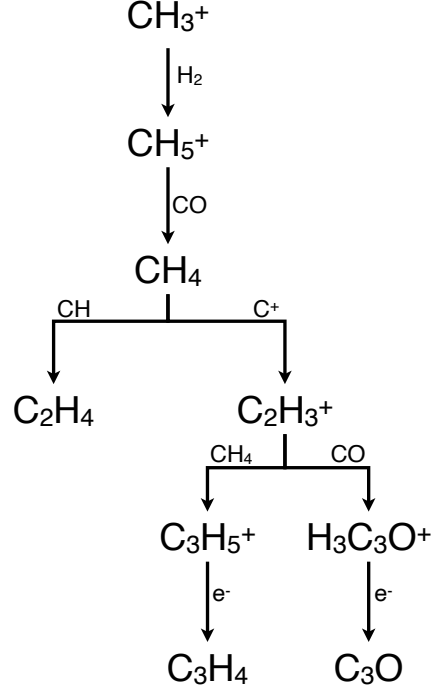


Figure 7. Example reactions for C bearing species. When a flare occurs, CH_3^+ and C^+ are enhanced (Figure 6) and drive further reactions in gas-phase carbon chemistry. Note that this reaction model is relevant in colder disk regions, within the H_2O snow-line. In warmer regions, CH_3^+ is quickly consumed by reacting with OH before Reaction 17 can occur.

phase cations, but a number of gas-phase neutral species, such as H_2O , are also impacted by flares.

The model suggests that X-ray flares can drive a new chemical steady state in some species, such as carbon chains. The long-term implications of flares is the topic of paper currently being prepared. Individual flares can drive observable variability in species such as HCO^+ , but the extent of observational implications has yet to be explored.

Prior to this work, flares have been considered negligible when modeling the chemical evolution of protoplanetary disks. Modeling flare driven chemistry give a more clear understanding the chemical origins of planetary systems and the history of potentially life sustaining molecules, and we find that biologically relevant molecules, such as carbon bearing species and oxygen bearing species, are dependent on flaring events.

5. ACKNOWLEDGEMENTS

This research is funded in support of the Virginia Space Grant Consortium and the National Science Foundation.

Additional thanks are given to Ilseore Cleeves, who has served as the project’s advisor.

References

1. Aikawa, Y., van Zadelhoff, G. J., van Dishoeck, E. F. & Herbst, E. Warm molecular layers in protoplanetary disks. *A&A* **386**, 622–632. eprint: [astro-ph/0202060](#) (May 2002).
2. Dutrey, A., Guilloteau, S. & Guelin, M. Chemistry of protosolar-like nebulae: The molecular content of the DM Tau and GG Tau disks. *A&A* **317**, L55–L58 (Jan. 1997).
3. Aikawa, Y. *et al.* Interferometric Observations of Formaldehyde in the Protoplanetary Disk around LkCa 15. *PASJ* **55**, 11–15. eprint: [astro-ph/0211440](#) (Feb. 2003).
4. Öberg, K. I. *et al.* The comet-like composition of a protoplanetary disk as revealed by complex cyanides. *Nature* **520**, 198–201. arXiv: [1505.06347](#) (Apr. 2015).
5. Walsh, C. *et al.* First Detection of Gas-phase Methanol in a Protoplanetary Disk. *ApJL* **823**, L10. arXiv: [1606.06492](#) [[astro-ph.EP](#)] (May 2016).
6. Ardila, D. R., Basri, G., Walter, F. M., Valenti, J. A. & Johns-Krull, C. M. Observations of T Tauri Stars Using the Hubble Space Telescope GHRS. II. Optical and Near-Ultraviolet Lines. *ApJ* **567**, 1013–1027 (Mar. 2002).
7. Bergin, E. A., Aikawa, Y., Blake, G. A. & van Dishoeck, E. F. The Chemical Evolution of Protoplanetary Disks. *Protostars and Planets V*, 751–766. eprint: [astro-ph/0603358](#) (2007).
8. Lynden-Bell, D. & Pringle, J. E. The evolution of viscous discs and the origin of the nebular variables. *MNRAS* **168**, 603–637 (Sept. 1974).
9. Henning, T. & Semenov, D. Chemistry in Protoplanetary Disks. *Chemical Reviews* **113**, 9016–9042. arXiv: [1310.3151](#) [[astro-ph.GA](#)] (Dec. 2013).
10. Williams, J. P. & Cieza, L. A. Protoplanetary Disks and Their Evolution. *ARA&A* **49**, 67–117. arXiv: [1103.0556](#) [[astro-ph.GA](#)] (Sept. 2011).
11. Cleeves, L. I. *et al.* The Coupled Physical Structure of Gas and Dust in the IM Lup Protoplanetary Disk. *ApJ* **832**, 110. arXiv: [1610.00715](#) [[astro-ph.SR](#)] (Dec. 2016).
12. Andrews, S. M. *et al.* The Disk Substructures at High Angular Resolution Project (DSHARP). I. Motivation, Sample, Calibration, and Overview. *ApJL* **869**, L41. arXiv: [1812.04040](#) [[astro-ph.SR](#)] (Dec. 2018).
13. Huang, J. *et al.* The Disk Substructures at High Angular Resolution Project (DSHARP). III. Spiral Structures in the Millimeter Continuum of the Elias 27, IM Lup, and WaOph 6 Disks. *ApJL* **869**, L43. arXiv: [1812.04193](#) [[astro-ph.SR](#)] (Dec. 2018).
14. Huang, J. *et al.* The Disk Substructures at High Angular Resolution Project (DSHARP). III. Spiral Structures in the Millimeter Continuum of the Elias 27, IM Lup, and WaOph 6 Disks. *ApJL* **869**, L43. arXiv: [1812.04193](#) [[astro-ph.SR](#)] (Dec. 2018).
15. Pérez, L. M. *et al.* The Disk Substructures at High Angular Resolution Project (DSHARP). X. Multiple Rings, a Misaligned Inner Disk, and a Bright Arc in the Disk around the T Tauri star HD 143006. *ApJL* **869**, L50. arXiv: [1812.04049](#) [[astro-ph.SR](#)] (Dec. 2018).
16. Dutrey, A. *et al.* Chemistry in disks. I. Deep search for N₂H⁺ in the protoplanetary disks around LkCa 15, MWC 480, and DM Tauri. *A&A* **464**, 615–623. eprint: [astro-ph/0612534](#) (Mar. 2007).
17. McGuire, B. A. 2018 Census of Interstellar, Circumstellar, Extragalactic, Protoplanetary Disk, and Exoplanetary Molecules. *ApJS* **239**, 17. arXiv: [1809.09132](#) [[astro-ph.GA](#)] (Dec. 2018).
18. Booth, A. S. *et al.* The First Detection of ¹³C¹⁷O in a Protoplanetary Disk: A Robust Tracer of Disk Gas Mass. *ApJL* **882**, L31. arXiv: [1908.05045](#) [[astro-ph.EP](#)] (Sept. 2019).
19. Belloche, A. *et al.* Re-exploring Molecular Complexity with ALMA (ReMoCA): interstellar detection of urea. *A&A* **628**, A10. arXiv: [1906.04614](#) [[astro-ph.GA](#)] (Aug. 2019).
20. Lee, K. L. K. *et al.* Gas phase detection and rotational spectroscopy of ethynethiol, HCCSH. *Molecular Physics* **117**, 1381–1391. arXiv: [1811.12798](#) [[astro-ph.GA](#)] (June 2019).
21. Strom, K. M., Strom, S. E., Edwards, S., Cabrit, S. & Skrutskie, M. F. Circumstellar material associated with solar-type pre-main-sequence stars - A possible constraint on the timescale for planet building. *AJ* **97**, 1451–1470 (May 1989).
22. Glassgold, A. E., Najita, J. & Igea, J. X-Ray Ionization of Protoplanetary Disks. *ApJ* **480**, 344–350 (May 1997).

23. Haisch Jr., K. E., Lada, E. A. & Lada, C. J. Disk Frequencies and Lifetimes in Young Clusters. *ApJL* **553**, L153–L156. eprint: [astro-ph/0104347](#) (June 2001).
24. Fedele, D., van den Ancker, M. E., Henning, T., Jayawardhana, R. & Oliveira, J. M. Timescale of mass accretion in pre-main-sequence stars. *A&A* **510**, A72. arXiv: [0911.3320 \[astro-ph.SR\]](#) (Feb. 2010).
25. Wolk, S. J. *et al.* Stellar Activity on the Young Suns of Orion: COUP Observations of K5-7 Pre-Main-Sequence Stars. *ApJS* **160**, 423–449. eprint: [astro-ph/0507151](#) (Oct. 2005).
26. Favata, F. *et al.* Bright X-Ray Flares in Orion Young Stars from COUP: Evidence for Star-Disk Magnetic Fields? *ApJS* **160**, 469–502. eprint: [astro-ph/0506134](#) (Oct. 2005).
27. Güdel, M. X-ray astronomy of stellar coronae. *A&A Rev* **12**, 71–237. arXiv: [astro-ph/0406661 \[astro-ph\]](#) (Sept. 2004).
28. Calvet, N., Patino, A., Magris, G. C. & D’Alessio, P. Irradiation of Accretion Disks around Young Objects. I. Near-Infrared CO Bands. *ApJ* **380**, 617 (Oct. 1991).
29. Bethell, T. J. & Bergin, E. A. The Propagation of Ly α in Evolving Protoplanetary Disks. *ApJ* **739**, 78. arXiv: [1107.3514 \[astro-ph.SR\]](#) (Oct. 2011).
30. Glassgold, A. E., Feigelson, E. D., Montmerle, T. & Wolk, S. *X-Ray Flares of Sun-like Young Stellar Objects and Their Effects on Protoplanetary Disks in Chondrites and the Protoplanetary Disk* (eds Krot, A. N., Scott, E. R. D. & Reipurth, B.) **341** (Dec. 2005), 165. arXiv: [astro-ph/0505562 \[astro-ph\]](#).
31. Maloney, P. R., Hollenbach, D. J. & Tielens, A. G. G. M. X-Ray-irradiated Molecular Gas. I. Physical Processes and General Results. *ApJ* **466**, 561 (July 1996).
32. Cleeves, L. I. *et al.* Variable H¹³CO⁺ Emission in the IM Lup Disk: X-ray Driven Time-Dependent Chemistry? *ArXiv e-prints*. arXiv: [1706.00833 \[astro-ph.SR\]](#) (June 2017).
33. Caramazza, M. *et al.* X-ray flares in Orion low-mass stars. *A&A* **471**, 645–654. arXiv: [0706.1500 \[astro-ph\]](#) (Aug. 2007).
34. Fogel, J. K. J., Bethell, T. J., Bergin, E. A., Calvet, N. & Semenov, D. Chemistry of a Protoplanetary Disk with Grain Settling and Ly α Radiation. *ApJ* **726**, 29. arXiv: [1011.0446 \[astro-ph.SR\]](#) (Jan. 2011).
35. Aikawa, Y., Umebayashi, T., Nakano, T. & Miyama, S. M. Evolution of Molecular Abundances in Protoplanetary Disks with Accretion Flow. *ApJ* **519**, 705–725 (July 1999).
36. Waggoner, A. R. & Cleeves, L. I. Modeling Time Dependent Water Chemistry Due to Powerful X-Ray Flares from T-Tauri Stars. *ApJ* **883**, 197. arXiv: [1908.08048 \[astro-ph.SR\]](#) (Oct. 2019).